



Rigorous model-based uncertainty quantification with application to terminal ballistics—Part II. Systems with uncontrollable inputs and large scatter

M. Adams, A. Lashgari, B. Li, M. McKerns, J. Mihaly, M. Ortiz*, H. Owhadi, A.J. Rosakis, M. Stalzer, T.J. Sullivan

Division of Engineering and Applied Science, California Institute of Technology, Pasadena, CA 91125, USA

ARTICLE INFO

Article history:

Received 23 August 2011
 Received in revised form
 1 December 2011
 Accepted 3 December 2011
 Available online 23 December 2011

Keywords:

Certification
 Uncertainty quantification
 Concentration of measure
 Terminal ballistics
 Martingale theory

ABSTRACT

This Part II of this series is concerned with establishing the feasibility of an *extended data-on-demand* (XDoD) uncertainty quantification (UQ) protocol based on concentration-of-measure inequalities and martingale theory. Specific aims are to establish the feasibility of the protocol and its basic properties, including the tightness of the predictions afforded by the protocol. The assessment is based on an application to terminal ballistics and a specific system configuration consisting of 6061-T6 aluminum plates struck by spherical 440c stainless steel projectiles at ballistic impact speeds in the range of 2.4–2.8 km/s. The system's inputs are the plate thickness, plate obliquity and impact velocity. The perforation area is chosen as the sole performance measure of the system. The objective of the UQ analysis is to certify the lethality of the projectile, i.e., that the projectile perforates the plate with high probability over a prespecified range of impact velocities, plate thicknesses and plate obliquities. All tests were conducted at Caltech's Small Particle Hypervelocity Range (SPHIR), which houses a two-stage gas gun. A feature of this facility is that the impact velocity, while amenable to precise measurement, cannot be controlled precisely but varies randomly according to a known probability density function. In addition, due to a competition between petalling and plugging mechanisms for the material system under consideration, the measured perforation area exhibits considerable scatter. The analysis establishes the feasibility of the XDoD UQ protocol as a rigorous yet practical approach for model-based certification of complex systems characterized by uncontrollable inputs and noisy experimental data.

© 2011 Elsevier Ltd. All rights reserved.

1. Introduction

In Part I of this sequence, we have demonstrated a *data-on-demand* (DoD) Uncertainty Quantification (UQ) protocol through an application to a deterministic and low-scatter system, namely, the assessment of lethality of S-2 tool steel projectiles against 6061-T6 aluminum plates at ballistic impact speeds, as realized at Caltech's GALCIT Powder-Gun Plate-Impact Facility. As stated in Part I, from the certification standpoint adopted in this work the general aim of UQ concerns the determination of tight upper bounds on the probability of failure of complex engineering systems. Specifically, *model-based* UQ is concerned with

* Corresponding author. Tel.: +1 626 395 4529.
 E-mail address: ortiz@aero.caltech.edu (M. Ortiz).

the determination of rigorous upper bounds on the probability of failure of the system with a maximum of computation and a minimum of testing.

The specific DoD UQ protocol assessed in Part I considers a deterministic response function $Y = G(X)$ that maps controllable system inputs X , i.e., system inputs whose value can be dialed precisely at will, to performance measures Y and relies on probability-of-failure upper bounds of the *concentration-of-measure* type (Boucheron et al., 2004a,b; McDiarmid, 1989a; Lugosi, 2006; Ledoux, 2001). If McDiarmid's inequality (McDiarmid, 1989a) is used to bound probabilities of failure, the system may then be certified on the sole knowledge of ranges of its input parameters—without *a priori* knowledge of their probability distributions, its mean performance $\mathbb{E}[Y] = M$ and a certain measure $D_G = U$ of the spread of the response, known as *system diameter*, which provides a rigorous quantitative measure of the uncertainty in the response of the system.

For the S2 steel/6061-T6 aluminum, the net outcome of the UQ analysis presented in Part I is an M/U confidence factor of 2.93, or a better than 99.9% confidence in the lethality of the projectiles over an impact velocity range of 200–400 m/s and plate thickness range of 0.81–1.62 mm. In addition, the determination of the modeling-error contribution to the system uncertainty, or modeling-error diameter, required a relatively small number (40) of tests-on-demand. This low data-on-demand requirement, in conjunction with the sole reliance on system input ranges and the good scaling properties of the protocol with the number of input parameters and performance measures, establishes the feasibility of the DoD UQ protocol as a rigorous yet practical approach for model-based certification of complex systems that are ostensibly deterministic and whose input parameters are controllable in the laboratory.

In this Part II of this article, we extend the DoD UQ protocol developed in Part I to systems with uncontrollable parameters and large scatter. We recall that the specific strategy adopted in Part I for integrating modeling and simulation into the UQ protocol relies on the seminorm property of function diameters. In this context, a model is regarded as a function $Y = F(X)$ that approximates the response $Y = G(X)$ of the system. An upper bound on the system diameter—and thus on the uncertainty in the response of the system—then follows from the triangular inequality $D_G \leq D_F + D_{G-F}$, and $U = D_F + D_{G-F}$ can be taken as a new—and conservative—measure of system uncertainty. In this approach, the total uncertainty of the system is the sum of the *predicted uncertainty*, i.e., the variability in performance predicted by the model as quantified by the model diameter D_F , and the *modeling-error uncertainty*, i.e., the discrepancy between model prediction and experiment as quantified by the modeling error diameter D_{F-G} . The calculation of the modeling-error diameter D_{F-G} requires the solution of a global optimization problem in which each evaluation of the objective function requires the simultaneous execution of a nominally identical simulation and experiment. The precise sequence of evaluations is determined by the algorithm used to solve the global optimization problem. However, this program fails when some of the input parameters are uncontrollable, i.e., their values cannot be dialed precisely in the course of an experiment. For such systems it is not possible to obtain data *on demand* for precisely preset values of the input parameters, as required by the data-on-demand protocol of Part I, and the protocol breaks down. *Noisy data*, or data exhibiting large scatter, may constitute an additional impediment to the application of the DoD UQ protocol of Part I, by rendering the response of the system stochastic. These impediments require a generalization of the CoM framework of Lucas et al. (2008), a generalization that we achieve in this Part II by an application of *martingale theory*.

As in Part I, a principal goal of the work presented in this Part II is to demonstrate the feasibility of the XDoD UQ protocol for uncertainty quantification by means of an actual example of application, namely, the terminal ballistics of 6061-T6 aluminum plates impacted by spherical 440c stainless steel projectiles at impact velocities in the range of 1.8 km/s to 3.1 km/s. All tests are conducted at Caltech's Small Particle Hypervelocity Range (SPHIR), which houses a two-stage gas gun. The system's inputs are the plate thickness and obliquity and impact velocity and, for simplicity, we choose the perforation area as the sole performance measure of the system. The objective of the uncertainty quantification analysis is to certify the *lethality* of the threat, i.e., that the projectile perforates the plate with high probability over a prespecified range of impact velocities and plate thicknesses and obliquities. An essential feature of the SPHIR facility is that the impact velocity, while amenable to precise measurement, cannot be controlled precisely but varies randomly according to a known probability density function. In addition, for the material system under consideration, the competition between petalling and plugging results in considerable scatter in the measured perforation area. Thus, the SPHIR facility and the 6061-T6 aluminum/440c stainless steel system provide an ideal testbed for the assessment of the XDoD UQ protocol. Overall, the assessment demonstrates the feasibility of the XDoD UQ protocol as a basis for rigorous certification, but also points to some limitations of the approach and suggests directions of further research and development.

2. Martingale inequalities and UQ

We recall that, following (Lucas et al., 2008), PoF upper bounds of the CoM type were formulated in Part I of this series by recourse to McDiarmid's inequality (McDiarmid, 1998, 1989b). In its simplest version, this inequality pertains to a system characterized by N real random inputs $X = (X_1, \dots, X_N) \in E \subseteq \mathbb{R}^N$ and a single real performance measure $Y \in \mathbb{R}$. Suppose that the function $G : \mathbb{R}^N \rightarrow \mathbb{R}$ describes the response function of the system. Suppose that the system fails when $Y \leq a$, where a is a threshold for the safe operation of the system. Then, a direct application of McDiarmid's inequality gives the following upper bound on the PoF of the system:

$$\mathbb{P}[G \leq a] \leq \exp\left(-2 \frac{M^2}{U^2}\right) \quad (1)$$

where

$$M = (\mathbb{E}[G] - a)_+ \quad (2a)$$

$$U = D_G \quad (2b)$$

are the *design margin* and the *system uncertainty*, respectively. In (2b), D_G is the diameter of the response function (cf. Part I, Section 2.1, for a definition of the diameter of a function). From (1) it follows that the system is certified if

$$\exp\left(-2\frac{M^2}{U^2}\right) \leq \epsilon \quad (3)$$

where ϵ is the PoF tolerance, or, equivalently, if

$$CF = \frac{M}{U} \geq \sqrt{\log\sqrt{\frac{1}{\epsilon}}} \quad (4)$$

where CF is the *confidence factor*. In writing (2a) and subsequently, we use the function $x_+ := \max(0, x)$. We see from the preceding expressions that McDiarmid's inequality supplies rigorous quantitative definitions of design margin and system uncertainty. In particular, the latter is measured by *system diameter* D_G , which measures the largest deviation in performance resulting from arbitrarily large perturbations of one input parameter at time. Within this simple framework, rigorous certification is achieved by the determination of two—and only two—quantities: the *mean performance* $\mathbb{E}[G]$ and the *system diameter* D_G . Extensions of McDiarmid's inequality to systems with multiple performance measures, unknown unknowns and to situations in which the mean performance is not known exactly, may be found in Lucas et al. (2008) and in Part I of this series.

We note that the calculation of the system diameter D_G requires the solution of the global optimization problem. In this problem, each evaluation of the objective function in turn requires two experiments, i.e., two evaluations of G . The precise sequence of evaluations is determined by the algorithm used to solve the global optimization problem. However, the execution of this program is compounded when some of the input parameters cannot be dialed precisely in the course of a test but vary randomly and uncontrollably. Thus, in this case it is impossible to obtain *data on demand*, as required by the global optimization algorithm, at deterministic values of the inputs and the scheme breaks down. This breakdown requires a generalization of the *data-on-demand* (DoD) UQ protocol of Part I, a generalization that we achieve in this Part II by an application of martingale theory.

2.1. Application to uncontrollable variables

We consider a system with random inputs (X, Z) of two types: known and *controllable variables* X and *uncontrollable or unknown variables* Z . The known controllable variables X can be dialed precisely in laboratory experiments. The known but uncontrollable variables cannot be dialed deterministically in laboratory tests and their values in particular tests are random with known distribution. Finally, we assume that the observed experimental scatter is the result of unknown random inputs, or unknown unknowns. As will become apparent, known uncontrollable inputs and unknown unknowns can conveniently be given an identical treatment within the martingale context. In particular, the uncontrollable random inputs and unknown unknowns are not assumed to be independent and may be correlated among themselves and to the controllable variables X .

The SPHIR facility described in Section 2 and the test configuration analyzed in Section 3.4 supply examples of these types of variables. Thus, the known inputs to the system are the plate thickness h , the plate obliquity α and the impact velocity v . The facility operates in such a way that the impact velocity in a given test cannot be dialed precisely but, instead, varies randomly with known probability density. Thus, in this case $X = (h, \alpha)$ is the set of known controllable inputs and v is a known uncontrollable input. In addition, the observed experimental scatter is attributed to unknown inputs which, together with v , comprise the input set Z .

For simplicity, we additionally assume a single performance measure Y of interest. Thus, within the present framework the response of the system is characterized by a function $Y = G(X, Z)$. Let $\langle G \rangle(X)$ denote the probability average of $G(X, Z)$ with respect to Z . The average with respect to the known but uncontrollable subset of Z can be performed using their known probability distributions. However, in practice averages with respect to unknown unknowns can only be determined by recourse to sampling. We additionally let $D_{\langle G \rangle}$ denote the McDiarmid diameter of $\langle G \rangle(X)$ (cf. Part I, Section 2.1, for a definition of the diameter of a function), which we shall refer to as the *averaged-system diameter*, and D_Z the maximum deviation from the averaged response, i.e.,

$$D_Z = \text{esssup}|G(X, Z) - \langle G \rangle(X)| \quad (5)$$

which we assume to be finite. Evidently, D_Z supplies a measure of the extent of experimental scatter in the data and, consequently, will be referred to as *experimental-scatter diameter*.

The following theorem supplies the sought probability-of-failure upper bound and follows immediately from Theorem 2.3 of McDiarmid (1997) (we also refer to the Theorem 6.7 and corollary 6.9 of McDiarmid (1989b), and to Appendix A for the main abstract result).

Theorem 2.1. Assume that the inputs X are statistically independent. Then we have almost surely that

$$\mathbb{P}[G(X,Z) \leq a] \leq \exp\left(-2 \frac{(\mathbb{E}[G]-a)_+^2}{D_{\langle G \rangle}^2 + D_Z^2}\right) \quad (6)$$

We note that inequality (6) is of the form

$$\mathbb{P}[G(X,Z) \leq a] \leq \exp\left(-2 \frac{M^2}{U^2}\right) \quad (7)$$

where

$$M = (\mathbb{E}[G]-a)_+ \quad (8a)$$

$$U = \sqrt{D_{\langle G \rangle}^2 + D_Z^2} \quad (8b)$$

may be regarded as the *system margin* and *system uncertainty*, respectively. Hence, a conservative certification criterion is obtained by requiring

$$\exp\left(-2 \frac{M}{U}\right) \leq \epsilon \quad (9)$$

where ϵ is a probability-of-failure tolerance. As in the DoD UQ protocol, we can turn inequality (9) around and rewrite the certification criterion in the form

$$CF = \frac{M}{U} \geq \sqrt{\log \sqrt{\frac{1}{\epsilon}}} \quad (10)$$

which becomes the new certification criterion. In this inequality CF is the *confidence factor* of the system.

Again, if follows from the preceding analysis that system can be rigorously certified solely on the sole basis of the mean performance $\mathbb{E}[G]$, the averaged-system diameter $D_{\langle G \rangle}$ and the experimental scatter diameter D_Z . For bound (10) to hold, only ranges of the known controllable parameters need to be known. As in the DoD UQ protocol, bound (10) supplies rigorous quantitative definitions of system margin and system uncertainty. In particular, the latter is measured by the root-mean-square of the averaged-system diameter $D_{\langle G \rangle}$ and the experimental-scatter diameter D_Z . This latter diameter is determined directly from test data and provides a measure of the uncertainty arising from the experimental scatter. As expected, large experimental scatter increases uncertainty and renders the system more difficult to certify. As in the DoD UQ protocol, the determination of the averaged-uncertainty diameter $D_{\langle G \rangle}$ requires the solution of a global optimization problem. In practice, the exact average response $\langle G \rangle(X)$ is not available and, therefore, we estimate it by means of an empirical mean

$$\langle G \rangle(X) \approx \mathbb{E}_n[G(X)] = \frac{1}{n} \sum_{i=1}^n G(X, Z_i) \quad (11)$$

where $\{Z_i\}_{i=1}^n$ are independent and identically distributed samples. Thus, in contrast to the DoD UQ protocol, every objective function evaluation necessitates the execution of a number of tests for the evaluation of the response function $\langle G \rangle$ averaged with respect to the known but uncontrollable and unknown inputs. The precise sequence of controllable variables required for the evaluation of $D_{\langle G \rangle}$ is determined by the optimization algorithm and it is not known *a priori*. Thus, the XDoD UQ protocol requires data-on-demand with respect to the known controllable inputs X but extends the DoD UQ protocol as regards the computation of averages of the response function with respect to the known but uncontrollable and unknown inputs.

2.2. Empirical mean estimation

As discussed in Part I (cf. also Lucas et al., 2008), the mean value $\mathbb{E}[G]$ of G under \mathbb{P} can be replaced by an empirical mean calculated using m independent and identically distributed samples of (X, Z) , albeit at the cost of a certain *margin hit*. More precisely, for any $\epsilon' > 0$ the probability-of-failure bound (7) and the certification criterion (10) hold true with probability at least $1-\epsilon'$ provided that we redefine the margin as

$$M = (\mathbb{E}_m[G]-a-\alpha)_+ \quad (12)$$

where $\mathbb{E}_m[G]$ denotes the empirical mean obtained from m independent and identically distributed samples, namely,

$$\mathbb{E}_m[G] = \frac{1}{m} \sum_{i=1}^m G(X_i, Z_i) \quad (13)$$

and

$$\alpha = U \sqrt{\frac{1}{2m} \log\left(\frac{1}{\epsilon'}\right)} \quad (14)$$

is a *margin hit* that compensates for the use of an empirical mean. Remarkably, the estimation of the exact mean by an empirical mean does not increase the uncertainty U of the system but, instead, has the effect of reducing the design margin M in the amount α . In particular, under-sampling of the mean response does not make the system more uncertain but, instead, makes the design less *robust*.

2.3. Model-based UQ

For complex systems, the execution of the XDoD UQ protocol based directly on experimental testing may require a large number of tests for the determination of the mean response $\langle G \rangle(X)$ and its diameter $D_{\langle G \rangle}$. Suppose, however, that a model $F(X, V)$ of the system is available, i.e., a function that maps all known inputs (X, V) , controllable (X) and uncontrollable $(V \subset Z)$, into performance measures and that approximates the actual averaged response function $\langle G \rangle(X)$ of the system. In the spirit of *model-based certification*, we wish to achieve rigorous certification with a maximum use of modeling and simulation and a minimum use of testing.

As in Part I, we accomplish this model integration by using the seminorm property of diameters and *triangulating between model and experiment*. In particular, we can triangulate *via* F and upper-bound the McDiarmid diameter of $\langle G \rangle$ as follows:

$$D_{\langle G \rangle} \leq D_{\langle F \rangle} + D_{\langle G-F \rangle} \quad (15)$$

The diameter $D_{\langle F \rangle}$ may be regarded as a *predicted averaged-model diameter*, which furnishes a measure of the variability of the averaged-system as predicted by the model. The diameter $D_{\langle G-F \rangle}$ may be regarded as an *averaged modeling-error diameter*, which supplies a measure of the discrepancy, or error, between model and experiment. The function F is a deterministic function with no unknown unknowns, and so $\langle F \rangle$ involves averaging only with respect to the known but uncontrollable inputs V . Again, in practice we approximate $\langle F \rangle(X)$ by means of the empirical mean

$$\langle F \rangle(X) \approx \mathbb{E}_i[F(X)] = \frac{1}{n} \sum_{i=1}^n F(X, V_i) \quad (16)$$

where $\{V_i\}_{i=1}^n$ are independent and identically distributed samples. The sample data V_i are chosen to match the sample data in the corresponding experimental evaluations of G . Hence, by the monotonicity of the exponential bound with respect to the diameter, for any $\epsilon' > 0$ the probability-of-failure bound (7) and the certification criterion (10) hold true with probability at least $1 - \epsilon'$ provided that we redefine the system uncertainty as

$$U = \sqrt{(D_{\langle F \rangle} + D_{\langle G-F \rangle})^2 + D_Z^2} \quad (17)$$

If, in addition, an empirical mean is used to estimate the mean response of the system, the reduced margin remains as in (12) with a margin hit of the form (14) in which U is given by (17).

It follows from these theoretical developments that a system with known but uncontrollable and unknown unknowns can be rigorously certified once the mean performance $\mathbb{E}[G]$, the predicted averaged-system diameter $D_{\langle F \rangle}$, the averaged modeling-error diameter $D_{\langle G-F \rangle}$ and the experimental-scatter diameter D_Z are known. In particular, the total uncertainty U aggregates three types of uncertainties: the uncertainty in the performance of the system as predicted by the model, measured by $D_{\langle F \rangle}$; the uncertainty due to the limited fidelity of the model, measured by $D_{\langle G-F \rangle}$; and the uncertainty due to the scatter in the experimental data, as measured by D_Z . The predicted uncertainty $D_{\langle F \rangle}$ is determined by exercising the model and may be regarded as the result of a nonlinear sensitivity analysis. In general, such predicted uncertainty by itself does not suffice for rigorous certification, as it does not account for the uncertainties due to the lack of fidelity of the model—the *badness* of the model—and uncertainties due to experimental scatter—the *badness* of the data. Evidently, numerous *ad hoc* measures of system sensitivity, model fidelity and experimental scatter can be contrived, and some of them might result in useful insights into uncertainties in system performance. What sets the present measures apart is that, together, they result in a rigorous upper bound on the probability of failure of the system and enable its rigorous certification.

2.4. Gaussian noise

The definition (5) of the experimental-scatter diameter as the maximum deviation from the averaged response may in some cases result in overly conservative upper bounds on the probability of failure. The upper bounds can be tightened if more information is known about the distribution of the experimental scatter. For instance, suppose that the scatter

$$\rho(X, Z) = G(X, Z) - \langle G \rangle(X) \quad (18)$$

is Gaussian. More precisely, we assume that $\langle G \rangle(X)$ and $\rho(X, Z)$ are independent and that ρ is a Gaussian random variable with variance σ^2 . Note that, in particular, the scatter distribution is not compactly supported and the maximum-deviation definition (5) of the experimental-scatter diameter diverges. Then (cf. [Theorem B.2](#), [Appendix B](#)), the bound (6) remains

valid with

$$D_z = 2\sigma \quad (19)$$

Thus, in the case of Gaussian noise, the experimental-scatter diameter equals twice the standard deviation of the noise.

3. Application to ballistic penetration

We proceed to demonstrate the feasibility and performance of the XDoD UQ protocol introduced in the foregoing by means of an application to terminal ballistics. The particular system under consideration consists of 6061-T6 aluminum plates struck spherical 440c stainless steel projectiles. The system's inputs are the plate thickness and impact velocity. For simplicity, we choose the perforation area as the sole performance measure of the system. The objective of the uncertainty quantification analysis is to certify the *lethality* of the projectile, i.e., that the projectile perforates the plate with high probability over a prespecified range of impact velocities and plate thicknesses.

3.1. Experimental facility and setup

All tests required for the determination of the modeling error diameter $D_{\langle G-F \rangle}$ were conducted at Caltech's Small Particle Hypervelocity Impact Range (SPHIR). This facility features a two-stage light gas gun with a 1.8 mm bore diameter launch tube, Fig. 1. The SPHIR facility and the experimental configuration considered in this study thus play several crucial roles as part of the uncertainty quantification analysis: they define the system to be certified and provide a specific and concrete realization of that system; the facility supplies the *data-on-demand* required for the computation of the modeling error diameter $D_{\langle G-F \rangle}$, cf. Section 3.4; and they provide an example of a system having uncontrollable inputs, namely, the impact velocity, and significant experimental scatter. A brief description of the facility follows for completeness.

3.1.1. Overall characteristics

Using 0.9 g of smokeless black powder propellant and helium or hydrogen gas at 150 psi pressure, the SPHIR facility is capable of producing mass-dependent velocities ranging from 2 to 10 km/s. Launch packages travel down a 3.6 m long flight tube into a $1 \times 1 \times 2$ m target chamber. The flight tube and the target chamber operate with a residual air pressure of approximately 1 Torr. The mounting system for target plates clamps to an approximately 75×25 mm area on the bottom edge of the target plate, leaving all other edges of the plate free. This mounting system enables the impact obliquity with respect to the target vertical axis to be adjusted. Impact obliquity is defined such that 0° corresponds to the target plate normal.

3.1.2. Experiment materials

In this work, 1.8 mm diameter 440c stainless steel spheres were used as impactors. Aluminum alloy 6061-T6 was selected as the target material. Large rectangular sheets of this alloy were first procured and then sheared into square target plates measuring 152×152 mm in dimension. A range of target plate thicknesses was initially selected based upon the results of a series of initialization experiments. Specific plate thicknesses were selected based upon availability.

3.1.3. Range performance

The SPHIR facility was used to accelerate the spherical 22.7 mg 440c stainless steel impactors to impact speeds ranging from 1.8 km/s to 3.1 km/s. At these impact speeds, impact kinetic energies ranging from approximately 35–100 J were achieved. Given the estimated 3.5 kJ of energy provided by the 0.9 g of smokeless black powder, these impact kinetic energies represent a 1–2.8% launch efficiency.

An essential limitation of the SPHIR facility is that the impact speed is not precisely controllable. For any shot conducted in the SPHIR facility, control over the impactor velocity can only be achieved through selection of the mass and geometry of the launch package. However, even with careful control of the launch package properties and other firing parameters, there exists an inherent random variability in the resulting impact speed. Fig. 2b presents the cumulative probability distribution of the impact speeds obtained from a series of 56 experiments conducted with the considered steel sphere impactor and identical launching parameters. If the two low outlier points are excluded, the distribution appears to be uniformly distributed between 2 and 3 km/s, which suggests an equal probability of obtaining any velocity in this range. However, including all points, a Gaussian distribution provides a better fit with a mean of 2.49 km/s and a standard deviation of 0.25 km/s.

3.1.4. Velocimetry

A Photron SA-1 FASTCAM high-speed camera is used to capture images of the impact event with a view to obtaining accurate measurements of the velocity of the projectile. Given the requirements for resolution, this camera can be operated with a framing rate up to 200,000 frames per second. The Photron camera is mounted above the target chamber looking down through a porthole such that the projectile passes through its field of view en-route to the target. A mirror located below the impactor shot-line and positioned to allow the impact event on the target to be visible by the camera.

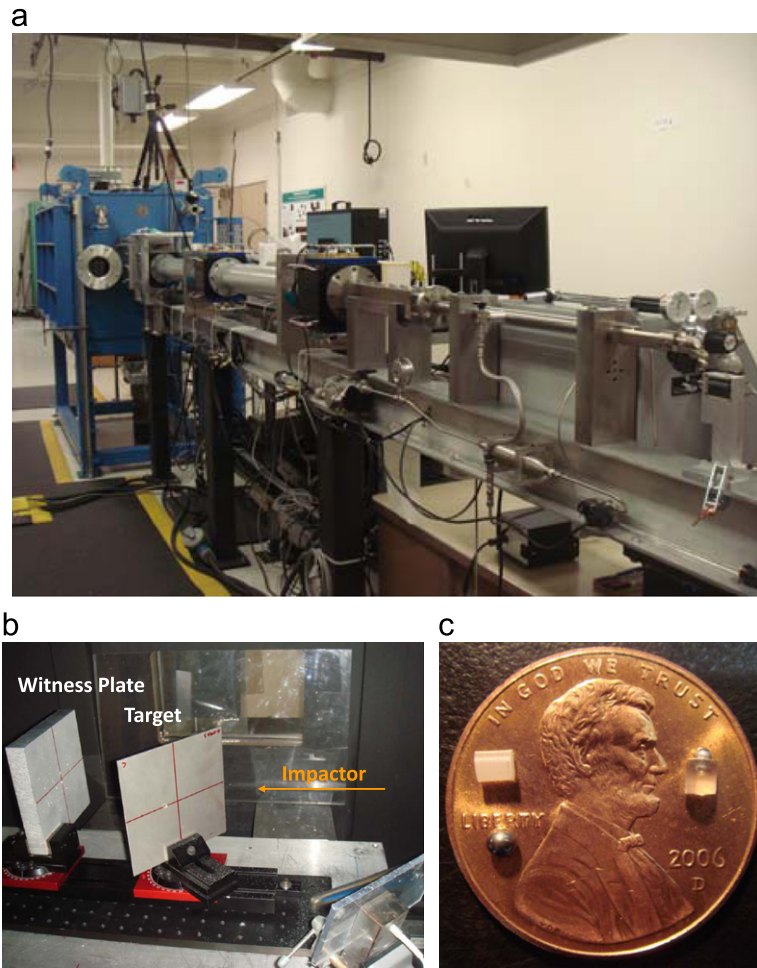


Fig. 1. Experimental set up. (a) General view of the Small Particle Hypervelocity Impact Range (SPHIR) Facility at Caltech. (b) 6061-T6 aluminum alloy target held in the evacuated chamber at the end of the gun barrel. (c) 440c stainless steel spherical projectiles and nylon sabots.

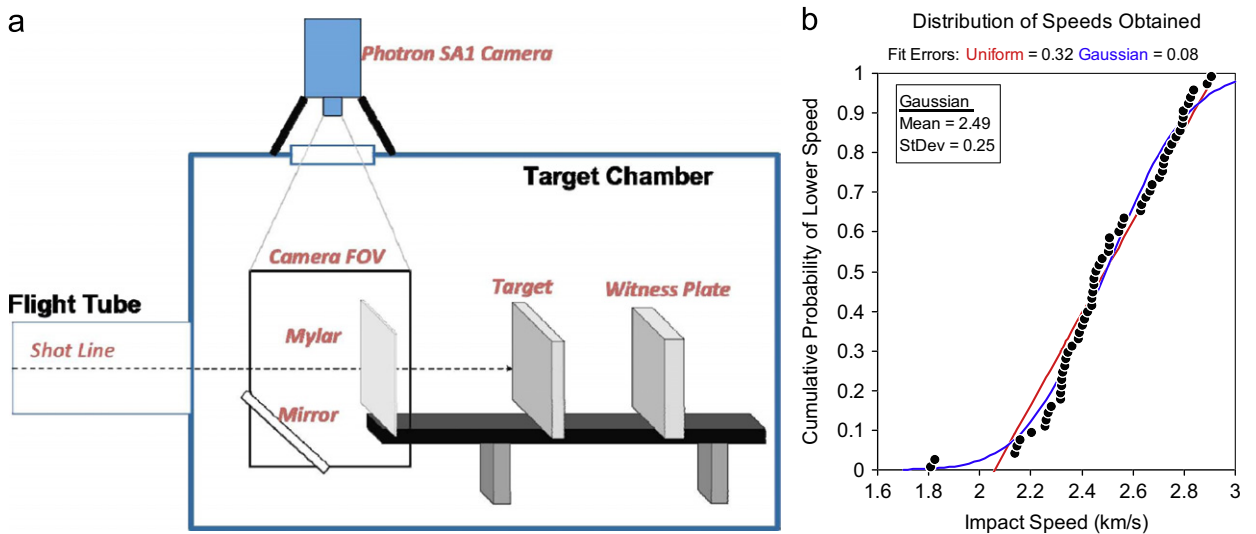


Fig. 2. (a) Target chamber configuration with Photron camera used to measure impactor speed. Impactor enters the target chamber from left through the flight tube. (b) The cumulative probability distribution of the impact speeds presented in figure 8, obtained for the 1.8 mm diameter 22.7 mg 440c stainless steel sphere impactor.

This setup is illustrated in Fig. 2. The Photron camera is triggered by a photo diode which is used to observe the impact flash on the target.

Application of the Photron camera to measure impact speed requires illumination of the impactor. However, given the small scale (1.8 mm) of the impactor and necessity of high framing rates for velocimetry accuracy, illumination of the impactor sphere is difficult. Furthermore, at this relatively low impact velocity, self-illumination of the impactor through ionization of the target chamber atmosphere is impractical. Consequently, to measure impactor speed, a 12.7 Micron thick Mylar sheet is placed in the camera field of view with its plane perpendicular to the velocity vector of the impactor. As the impactor passes through the Mylar, it produces a bright flash adequate for the camera to image. The thin Mylar sheet produces little or no damage to the steel ball at these perforation speeds. The Mylar sheet is located a fixed distance from the target and the impactor velocity is determined from this distance and the time-of-flight between the Mylar and target impact flashes. The uncertainty of the position of the Target and the Mylar is small, less than 3 mm; hence, the major uncertainty in the velocity measurement is determined primarily by the framing rate of the high-speed camera. With the framing rate of 200,000 fps used in this campaign, uncertainties in measured values of impact speed are on the order of 2%.

3.1.5. Initialization experiments

The selection of ranges for target thicknesses and obliquities considered in this UQ campaign first required an understanding of the ballistic limit behavior of the steel sphere impactor and aluminum target configuration. Here, the ballistic limit refers to the impact speed at which perforation is first achieved for a given target thickness and obliquity. A series of initialization experiments was conducted to determine the ballistic limit velocity for aluminum plates of varying thickness as a function of impact obliquity. Based on these experiments, a model was created to describe the ballistic limit velocity as a function of target thickness and impact obliquity. The ballistic limit model played an important role in the *robust design* of the system, e.g., in the selection of an impact velocity range resulting in large *margin-to-uncertainty*, or M/U , ratios.

3.1.6. Experimental results

Typical images of a perforated plate are shown in Fig. 3a. As in Part I, an Optimet MiniConoscan 3000 Conoscope system was used to measure post-mortem perforation areas. A typical image of a scanned surface of a perforated plate is shown in Fig. 3b. Selected perforation area data are also plotted in Fig. 4a as a function of projectile velocity for different plate thickness and incidence angles. In contrast to the system considered in Part I, the data now exhibit considerable scatter. This scatter is a consequence of the competition between two main perforation mechanisms that operate in the range of impact velocities under consideration, namely, *petalling* and *plugging*. Thus, near the ballistic limit perforation is dominated by the petalling mechanism, as radial cracks form and open under the impactor. This process is very sensitive to small changes in material properties or impact conditions and can therefore lead to variations in perforation area of more than 50% for nominally replicated experiments. As the impact velocity increases well above the ballistic limit, a shear plugging mechanism dominates the perforation resulting in the least amount of observed scatter.

3.1.7. A surrogate model

The feasibility of executing the DoD UQ protocol with experiments conducted *in real time*, i.e., simultaneously with the rest UQ analysis, has been assessed in Part I of this study. In this Part II, in order to facilitate the analysis and the assessment of different optimization algorithms, we have carried out all UQ analyses using a *surrogate model* of the SPHIR experimental facility. However, it bears emphasis that the use of surrogate models is not an essential part of the DoD or XDoD protocols and is adopted here as a matter of convenience. Indeed, as we shall see, the UQ analysis presented in Section 3.4 required 96 experiments (cf. Section 4) and, therefore, it could also have been done carrying out the experiments in real time.

The surrogate model is constructed in two steps. Firstly, we construct a deterministic surrogate that aims at fitting the mean response of the system. Secondly, we superimpose Gaussian noise on the deterministic model. Over the range of

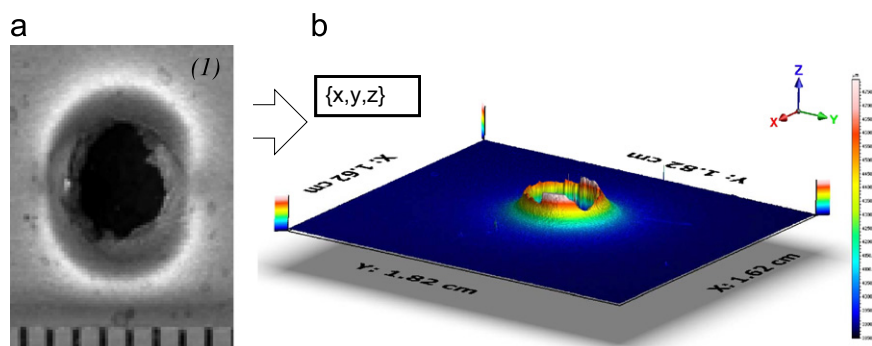


Fig. 3. Typical images of the perforated 6061-T6 aluminum plate: (a) impact face, (b) scanned profile.

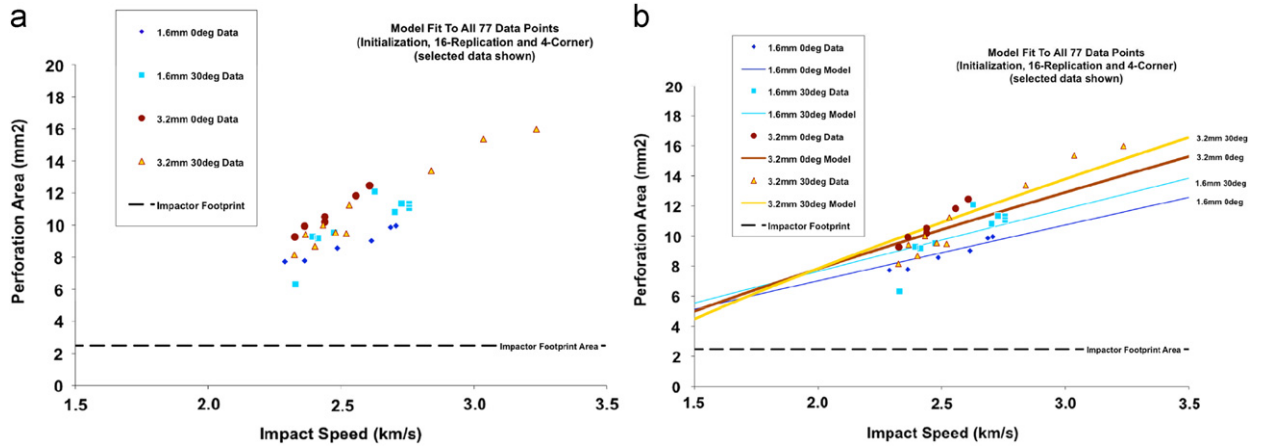


Fig. 4. (a) Selected perforation area data used in the uncertainty quantification analysis. (b) Surrogate fit to the impact velocity range of 2.4–2.8 km/s.

Table 1

Surrogate model constants fitted to impact velocities in the range of 2.4–2.8 km/s.

A_0 (mm ²)	D (mm)	v_0 (km/s)	α_0 (°)	a_0	b_0	α_1 (°)	a_1	b_1
4.450	1.778	6.412	23.64	−0.6596	8.141	10.98	−0.6279	−2.539

interest, namely, an impact velocity range $v \in [2.4, 2.8]$ km s^{−1}, a plate thickness range $h \in [1.6, 3.2]$ mm and a plate obliquity range $\alpha \in [0^\circ, 30^\circ]$, the mean perforation area (in mm²) is well-described by the polynomial fit

$$\frac{G_S(h, \alpha, v)}{A_0} = \left(1 + \frac{\alpha}{\alpha_0} \left(1 + a_0 \frac{h}{D}\right)\right) \left(1 + b_0 \frac{h}{D}\right) \frac{v}{v_0} + \left(1 + \frac{\alpha}{\alpha_1} \left(1 + a_1 \frac{h}{D}\right)\right) \left(1 + b_1 \frac{h}{D}\right) \quad (20)$$

where $D=1.778$ mm is the diameter of the impactor and the remaining fitting constants are tabulated in Table 1.

An additive noise model is superimposed on the deterministic surrogate in order to account for the deviations of the system from the deterministic surrogate model G_S . These deviations are essentially random in nature. The empirical cumulative distribution functions for the scatter $G(h, \alpha, v) - G_S(h, \alpha, v)$, at the *four corners* of the thickness–obliquity operating range, are shown in Fig. 5. Interestingly, the statistical properties of the scatter are different in each of the four corners, particularly at high impact obliquity. However, the scatter for the complete four corners data set, which includes 29 experiments, is reasonably well represented by a normal distribution with mean $\mu = -0.35$ mm² and standard deviation $\sigma = 0.7$ mm². Therefore, the complete noisy surrogate model is

$$G_{NS}(h, \alpha, v) = G_S(h, \alpha, v) + \mathcal{N}(\mu, \sigma) \quad (21)$$

where $\mathcal{N}(\mu, \sigma)$ denotes a normally distributed (Gaussian) random variable with mean μ and standard deviation σ .

It should be carefully noted that we do not claim that certification of G_{NS} is equivalent to certification of the experimental system G , only that G_{NS} is a system that is qualitatively similar—in trend and in noisiness—to G . Consequently, the XDoD UQ protocol can indeed be equivalently demonstrated based on either the experimental system G or its noisy surrogate G_{NS} .

3.2. Computational model

All calculations are carried out using the Optimal-Transportation MeshFree (OTM) method of Li et al. (2010) extended to account for contact and fracture (cf. Schmidt et al., 2009) (cf. Part I, Section 3.2). A detailed description of the OTM terminal ballistic model employed in the present work may be found in Li et al. (2012). In all calculations, the materials for the target and projectile are described by means of J_2 -viscoplasticity models with power-law hardening, rate-sensitivity and thermal softening (cf., e.g., Camacho and Ortiz, 1997; Yadav et al., 2001). Specifically, the rate-sensitivity law is assumed to be of the form for the target

$$\dot{\epsilon}^p = \dot{\epsilon}_0^p \left(\frac{\sigma - \sigma_c(\epsilon^p, T)}{\sigma_0} \right)^m \quad (22)$$

where ϵ^p is the Mises effective plastic strain, σ is a Mises effective stress, T is the absolute temperature, $\dot{\epsilon}_0^p$ is a reference effective plastic-strain rate, σ_0 is a reference stress and m is the rate-sensitivity exponent. The critical stress for plastic

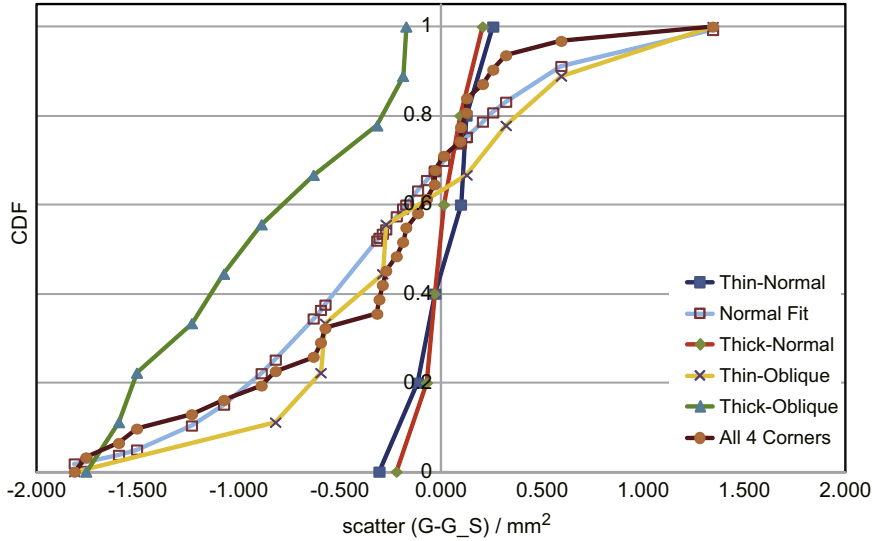


Fig. 5. The empirical cumulative distribution functions for the four corner data set, both grouped according to plate thickness and obliquity, and aggregated, along with the normal fit.

yielding is assumed of the form

$$\sigma_c(\epsilon^p, T) = Y(T) \left[1 + \left(\frac{\epsilon^p}{\epsilon_0^p} \right)^{1/n} \right] \tag{23}$$

where $Y(T)$ is the yield stress, ϵ_0^p is a reference effective plastic strain, and n is the hardening exponent. Finally, the yield stress is assumed of the form

$$Y(T) = \sigma_y \left(1 - \frac{T - T_0}{T_m - T_0} \right)^l \tag{24}$$

where σ_y is the yield stress at reference absolute temperature, T_0 and T_m is the reference and melting temperature, respectively, and l is the thermal softening exponent.

However, in a typical high-speed impact event, a power viscosity law with constant rate sensitivity is not adequate for structural steels (Marusich and Ortiz, 1995). The experimental stress–strain curves (Klopp et al., 1985; Clifton and Klopp, 1985; Tong et al., 1992) for the structural steels exhibit a transition at strain rates of the order of 10^5 – 10^6 s⁻¹ which may be attained in the projectile during impact. The accurate modeling of this type of behavior is of the essence, since a high rate sensitivity in the projectile may lead to an elevation in stress which in turn can promote brittle fracture and result in bigger perforation areas. Therefore, the stepwise rate-sensitivity law (Marusich and Ortiz, 1995)

$$\dot{\epsilon}^p = \dot{\epsilon}_0^p \left(\frac{\sigma - \sigma_c(\epsilon^p, T)}{\sigma_0} \right)^{m_1} \quad \text{if } \dot{\epsilon}^p \leq \dot{\epsilon}_t \tag{25a}$$

$$\dot{\epsilon}^p = \left(\frac{\dot{\epsilon}_0^p}{\dot{\epsilon}_t} \right)^{m_2/m_1 - 1} \left(\frac{\sigma - \sigma_c(\epsilon^p, T)}{\sigma_0} \right)^{m_2} \quad \text{if } \dot{\epsilon}^p > \dot{\epsilon}_t \tag{25b}$$

is employed for the projectile, where m_1 and m_2 are low and high strain rate sensitivity exponents and $\dot{\epsilon}_t$ is the threshold strain rate which separates the two regimes, the other variables are the same as those in the constitutive relations of the target.

The elastic response for the projectile and target is assumed to be quadratic in the elastic logarithmic strains, with isotropic elastic coefficients depending linearly on temperature and vanishing at the melting temperature. The equation of state, which governs the volumetric response of the material, is assumed to be of the Mie-Grüneisen type.

Under ballistic impact conditions, the temperature increase experienced by the projectile/target may be significant, which necessitates the concurrent solution of the mechanical and thermal field equations. In this work we assume adiabatic heating, with heat generated due to plastic work only. Specifically, we compute the rate of heating per unit undeformed volume as

$$S = \beta \dot{W}^p \tag{26}$$

where β is the Taylor–Quinney coefficient and \dot{W}^p is the plastic power per unit deformed volume. The effect of the rate of adiabatic heating on ballistic performance has been investigated in Yadav et al. (2001). Higher-fidelity models of adiabatic

heating accounting for its dependence on deformation, deformation rate and temperature are available (Hodowany et al., 2000; Stainier and Ortiz, 2010; Yang et al., 2006), but such enhancements are beyond the scope of the present work. The material parameters have been chosen according to relevant literature Yadav et al. (2001) and collected in Tables 2–4. The rate sensitivity behavior of Al6061-T6 at high strain rate above 10^3 s^{-1} is described by Yadav et al. (1995).

Fig. 6 shows a snapshot at $3.0 \mu\text{s}$ of a calculation corresponding to an impact velocity $v=2.4 \text{ km/s}$, a plate thickness $h=2.286 \text{ mm}$, and plate obliquity $\alpha = 0^\circ$. Fig. 6a shows the nodal set color coded according to von-Mises stress, and Fig. 6b shows the material point set colored according to the local energy-release rate computed by means of the *eigenfracture* method (Schmidt et al., 2009). It is evident from these figures that the plate is defeated by a plugging mechanism accompanied by extensive plastic deformation in both the plate and the projectile. Indeed, as a result of adiabatic heating the plastic deformations localize to a cylindrical through-thickness shear band, Fig. 6a, and ductile fracture subsequently occurs along the shear band, Fig. 6b, resulting in the perforation of the plate.

A comparison between perforation areas computed from the velocity-averaged surrogate (surface) and OTM calculations (dots) are shown in Fig. 7 as a function of plate thickness and obliquity. Specifically, the surface in the figure is obtained by averaging the deterministic surrogate $G_S(h, \alpha, v)$, Eq. (19), with respect to the impact velocity v assuming a uniform distribution over the range $[2.4, 2.8] \text{ km/s}$. The OTM results are generated using random impact velocities sampled according to the same probability observed distribution. As may be seen from the figure, the OTM perforation areas capture the overall trend defined by the velocity-averaged deterministic surrogate.

3.3. Optimization and computation of diameters

The computation of diameters requires the solution of a global optimization problem over the operating range of the input parameters. Global search algorithms often require inordinately large numbers of iterations and function evaluations in order to find a global optimum. In Part I of this series, the *lattice*-Powell method (McKerns and Aivazis, 2010) is used as a fast algorithm to discover the global optima for a deterministic system with controllable inputs and small scatter. The *lattice*-Powell method utilizes parallel computing to simultaneously launch N Powell's optimizers (Powell, 1989, 1994), each starting from different initial starting points in input parameter space. The *lattice*-Powell method effectively cuts down on the number of iterations to convergence, but the number function evaluations can explode as N is increased. The evaluation of a modeling-error diameter, such as D_{F-G} , requires an experiment $G(X)$ to be performed at a set of input parameters determined by the optimizer, whenever a function evaluation is required by the optimizer. In Part I, we utilize a surrogate function G_S in lieu of G in order to obtain a good initial set of starting points for the evaluation of D_{F-G} , which greatly decreases the number of iterations to convergence and, consequently, the number of experiments required.

For systems with uncontrollable inputs and large scatter, such as considered in this Part II, the response function is not deterministic and the DoD UQ protocol of Part I needs to be modified accordingly, leading to the formulation of an extended XDoD UQ protocol. The main difference between the DoD and the XDoD protocols is that the former works with a deterministic response function and a deterministic model, G and F , respectively, whereas the latter works with an averaged response function and an averaged model, $\langle G \rangle$ and $\langle F \rangle$, respectively. In the calculations presented in Section 3.4, the averaging is carried out by sampling, Eqs. (11), with sample size n chosen so as to render the sampling error

Table 2

Mechanical material constants for the plate.

ρ (kg/m ³)	E (GPa)	ν	σ_0 (MPa)	ϵ_0^p	n	$\dot{\epsilon}_0^p$	m
2700	69	0.33	276	0.001	13.5	1000	11.5

Table 3

Mechanical material constants for the projectile.

ρ (kg/m ³)	E (GPa)	ν	σ_0 (MPa)	ϵ_0^p	n	$\dot{\epsilon}_0^p$	m_1	m_2	$\dot{\epsilon}_t$ (s ⁻¹)
7650	200	0.3	1090	0.001	22	1	100	5	2×10^5

Table 4

Thermal constants.

Material	c (J/kg K)	T_0 (K)	T_m (K)	l	β
Al6061-T6	896	298	853	0.5	0.9
Stainless steel 440c	477	298	1777	1.17	0.9

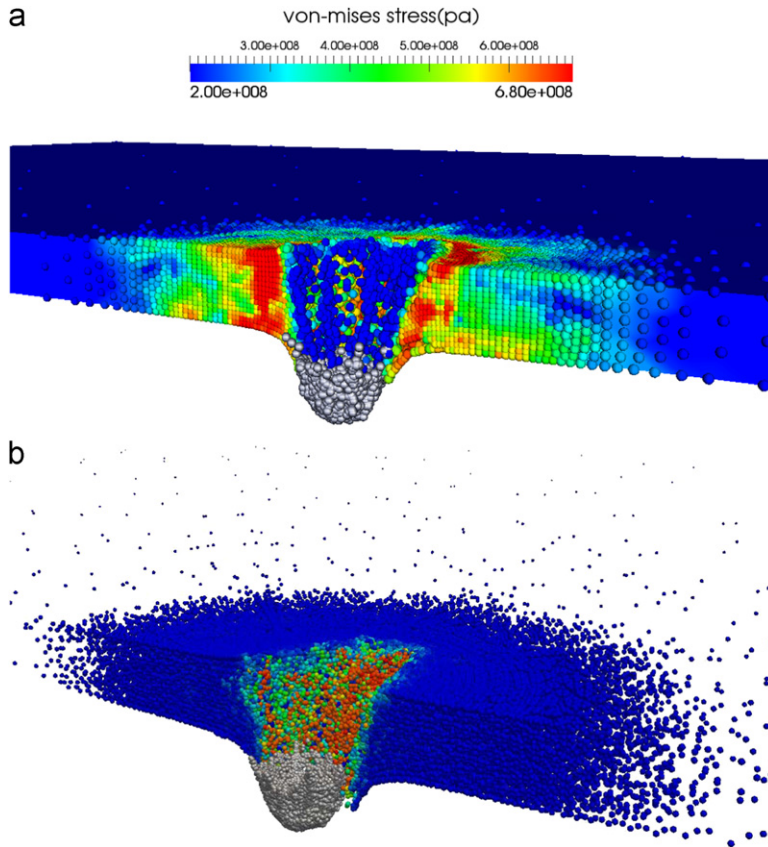


Fig. 6. Snapshot of aluminum plate after perforation by steel sphere (colored gray) at $3.0 \mu\text{s}$ after impact. Plate thickness $h=2.286 \text{ mm}$, plate obliquity $\alpha=0^\circ$ and impact velocity $v=2.4 \text{ km/s}$. (a) Nodal point set and level contours of von Mises effective stress. (b) Material point set and level contours of local energy-release rate, or ‘driving force’ for fracture, computed by means of the *eigenfracture* method (Schmidt et al., 2009).

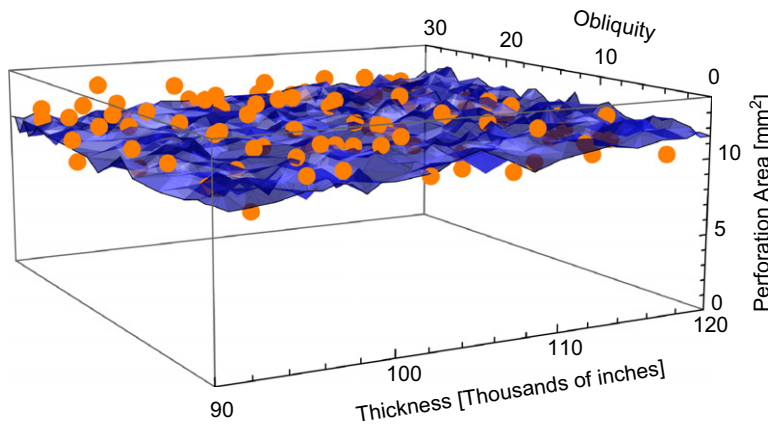


Fig. 7. Comparison between perforation areas computed from velocity-averaged surrogate (surface) and OTM calculations (dots) as a function of plate thickness and obliquity. The OTM results are generated using random impact velocities generated according to the experimentally observed distribution.

negligible. However, once the averaging with respect to uncontrollable inputs and experimental scatter is effected, resulting in the averaged functions $\langle G \rangle$ and $\langle F \rangle$, the calculation of the predicted averaged-system diameter $D_{\langle F \rangle}$ and averaged modeling-error diameter $D_{\langle G-F \rangle}$ is identical to the calculation of their deterministic counterparts D_F and D_{G-F} , respectively, as discussed in Part I. As discussed in Section 3.1.7, in calculations we use a noisy surrogate G_{NS} in lieu of G and assume that the scatter is Gaussian (21) as a matter of convenience and for ease of assessing various optimization algorithms. In particular, in addition to the lattice-Powell algorithm we have assessed the performance of the *buckshot-Powell* algorithm. Buckshot-Powell is a variant on the lattice-Powell optimizer, where the starting points for the N

optimizers are selected at random from a uniform distribution over input parameter space, instead of starting the N optimizers on a regular grid. The buckshot-Powell algorithm introduces an additional element of randomness into the procedure through the choice of the initial starting points. While the number of iterations required for this method remains of the same order as that required by the lattice-Powell method, the number of function evaluations required is now randomized. In general, buckshot-Powell also performs similarly to lattice-Powell as regards the number of function evaluations.

3.4. UQ analysis

In this section, we apply the XDoD UQ protocol to the plate/projectile system defined in Section 3.1. We recall that this system consists of Al 6061-T6 plates struck at oblique incidence by 1.8 mm diameter 440c stainless steel spheres. We take the inputs to the system to be the plate thickness h , the plate obliquity α and the impact velocity v . Within the experimental configuration adopted in this study, the impact velocity is uncontrollable and varies randomly according to an ostensibly uniform distribution between 2 and 3 km/s. The plate thickness is assumed to take values in the interval $[90 \text{ mills}, 125 \text{ mills}] \equiv E_h$, the plate obliquity in the interval $\alpha \in [0^\circ, 30^\circ] \equiv E_\alpha$ and the impact velocity in the interval $[2.4 \text{ km/s}, 2.8 \text{ km/s}] \equiv E_v$. No information other than their ranges E_h and E_α is presumed known regarding the distribution of the plate thickness and obliquity. The UQ analysis is carried out using the noisy surrogate (21) as fitted to experimental data acquired in Caltech's Small Particle Hypervelocity Impact Range (SPHIR), cf. Section 3.1. All calculations employ the Optimal Transportation Meshfree (OTM) method (Li et al., 2010) extended to account for contact and fracture (Schmidt et al., 2009), cf. Section 3.2.

We recall (cf. Section 2) that, with probability $1 - \epsilon'$, the probability of failure of the system is bounded by (Theorem 2.1)

$$\mathbb{P}[G(h, \alpha, v, Z) = 0] \leq \exp\left(-2 \frac{M^2}{U^2}\right) \quad (27)$$

where

$$M = (\mathbb{E}_m[G] - a - \alpha)_+ \quad (28a)$$

$$U = \sqrt{(D_{\langle F \rangle} + D_{\langle G-F \rangle})^2 + D_Z^2} \quad (28b)$$

are the system margin and uncertainty, respectively,

$$\mathbb{E}_m[G] = \frac{1}{m} \sum_{i=1}^m G(h_i, \alpha_i, v_i, Z_i) \quad (29a)$$

$$\alpha = U \sqrt{\frac{1}{2m} \log\left(\frac{1}{\epsilon'}\right)} \quad (29b)$$

are the empirical mean obtained from experimental samples and the corresponding margin hit, respectively,

$$\langle G \rangle(h, \alpha) = \frac{1}{n} \sum_{i=1}^n G(h, \alpha, v_i) \quad (30a)$$

$$\langle F \rangle(h, \alpha) = \frac{1}{n} \sum_{i=1}^n F(h, \alpha, v_i) \quad (30b)$$

are the system response and model response averaged over the assumed operating range $[2.4 \text{ km/s}, 2.8 \text{ km/s}]$ with respect to an impact velocity uniformly distributed over the interval $[2 \text{ km/s}, 3 \text{ km/s}]$,

$$D_{\langle F \rangle} = \sqrt{(D_{\langle F \rangle}^h)^2 + (D_{\langle F \rangle}^\alpha)^2} \quad (31a)$$

$$D_{\langle G-F \rangle} = \sqrt{(D_{\langle G-F \rangle}^h)^2 + (D_{\langle G-F \rangle}^\alpha)^2} \quad (31b)$$

are the predicted averaged-system diameter and modeling-error diameter, respectively,

$$D_{\langle F \rangle}^h = \sup_{\substack{h, h' \in E_h \\ \alpha \in E_\alpha}} |\langle F \rangle(h, \alpha) - \langle F \rangle(h', \alpha)| \quad (32a)$$

$$D_{\langle F \rangle}^\alpha = \sup_{\substack{\alpha, \alpha' \in E_\alpha \\ h \in E_h}} |\langle F \rangle(h, \alpha) - \langle F \rangle(h, \alpha')| \quad (32b)$$

$$D_{\langle G-F \rangle}^h = \sup_{\substack{h, h' \in E_h \\ \alpha \in E_\alpha}} |\langle G-F \rangle(h, \alpha) - \langle G-F \rangle(h', \alpha)| \quad (32c)$$

$$D_{\langle G-F \rangle}^z = \sup_{\substack{\alpha, \alpha' \in \mathbb{E}_z \\ h \in \mathbb{E}_h}} |\langle G-F \rangle(h, \alpha) - \langle G-F \rangle(h, \alpha')| \quad (32d)$$

are the corresponding subdiameters with respect to the plate thickness and plate obliquity, respectively. In calculations, the empirical means (29) is calculated using a sample of 50 points, and (30) using 10 points, i.e., $m=50$ and $n=10$. In all the preceding expressions, we use the noisy surrogate (21) in lieu of the experimental response G as a matter of convenience. By virtue of the Gaussian character of the noise in the surrogate model, the experimental-scatter diameter follows as:

$$D_Z = 2\sigma \quad (33)$$

where $\sigma = 0.7 \text{ mm}^2$ is the standard deviation of the experimental scatter.

We note that, owing to the simple structure of the noisy surrogate and the uniform distribution of the impact velocities we have, explicitly, $\langle G_{NS} \rangle(h, \alpha) = G_S(h, \alpha, \bar{v}) + \mu$, where $\bar{v} = 2.6 \text{ km/s}$ is the mean value of the impact velocity distribution and $\mu = -0.35 \text{ mm}^2$ is the mean value of the scatter. However, for purposes of assessing the general procedure in calculations we do not avail ourselves of these identities and directly use the empirical means defined in the foregoing.

The results of the UQ analysis are summarized in Table 5. The average perforation area over the chosen operating range, computed through an empirical mean based on a sample of size 50, is 11.17 mm^2 . The margin hit due to estimation of mean performance by an empirical mean is 1.5 mm^2 . The total averaged-model diameter $D_{\langle F \rangle}$, which measures the variability of the perforation area as predicted by the model, is computed to be 4.86 mm^2 , which is a substantial fraction of the average perforation area. Thus, the model predicts a substantial variation of the perforation area over the entire range of impact velocities and plate thicknesses. Likewise the total averaged modeling-error diameter $D_{\langle F-G \rangle}$, which measures the ‘badness’ of the model as compared with experiment, is computed to be 4.50 mm^2 , which is also a substantial fraction of the average perforation area. This relatively large value of the averaged modeling-error diameter $D_{\langle F-G \rangle}$ is indicative of systematic modeling errors. Finally, the experimental scatter diameter D_Z , which measures extent of the scatter in the experimental data, is 3.89 mm^2 , which, while substantial, is smaller than both the averaged-model diameter and the averaged modeling-error diameter. The total perforation-area uncertainty is $U = \sqrt{(D_{\langle F \rangle} + D_{\langle F-G \rangle})^2 + D_Z^2} = 10.13 \text{ mm}^2$, whereas the total margin is $M = (\hat{\mathbb{E}}_m[G] - \alpha)_+ = 9.67 \text{ mm}^2$, which gives an M/U ratio, or confidence factor, of 0.95, or a probability-of-failure upper bound of 16.2%.

Evidently, the probability-of-failure upper bound thus computed is overly conservative. Several factors contribute to the laxity of the bound. Thus, the triangulation between model and experiment introduces a first element of conservatism. In order to estimate the loss of tightness due to this triangulation, we note that for the system under consideration it is possible to calculate directly the averaged-system diameter $D_{\langle G \rangle}$. The resulting subdiameters are $D_{\langle G \rangle}^h = 4.52 \text{ mm}^2$ and $D_{\langle G \rangle}^z = 2.54 \text{ mm}^2$, jointly giving a diameter $D_{\langle G \rangle} = 5.18 \text{ mm}^2$. Evidently, this diameter is substantially smaller than the upper bound $D_{\langle F \rangle} + D_{\langle F-G \rangle} = 9.36 \text{ mm}^2$ delivered by the triangular inequality. Indeed, using $D_{\langle G \rangle}$ gives a total uncertainty $U = \sqrt{D_{\langle G \rangle}^2 + D_Z^2} = 6.48 \text{ mm}^2$, substantially smaller than before, a confidence factor $M/U = 1.4$ and a probability-of-failure upper bound of 2%, also substantially smaller than before. Thus, much of the laxity of the triangulated probability-of-failure upper bound may be attributed to modeling error, which is found to be largest and of the order of 10% of the perforation area at low obliquity angles.

Tighter upper bounds on the probability of non-perforation can be systematically obtained, albeit at increasing experimental and computational cost, by partitioning the input parameter domain, as in Sullivan et al. (2011). We

Table 5

Summary of results from the UQ analysis of a spherical 440c stainless steel projectiles/6061-T6 aluminum plate system. Plate thicknesses are in the range [2.2 mm, 3.2 mm], obliquities in the range [0°, 30°] and impact velocities in the range [2.4 km/s, 2.8 km/s].

Model diameter $D_{\langle F \rangle}$	
Thickness	3.46 mm ²
Obliquity	3.42 mm ²
Total	4.86 mm ²
Modeling-error diameter $D_{\langle F-G \rangle}$	
Thickness	3.50 mm ²
Obliquity	2.80 mm ²
Total	4.50 mm ²
Experimental scatter diameter D_Z	
	3.89 mm ²
Total uncertainty $U = \sqrt{(D_{\langle F \rangle} + D_{\langle F-G \rangle})^2 + D_Z^2}$	
	10.13 mm ²
Empirical mean $\mathbb{E}_m[G]$, $m=50$	
	11.17 mm ²
Margin hit α ($\epsilon' = 1\%$)	
	1.5 mm ²
Confidence factor M/U	
	0.95
PoF upper bound	
	16.2%

Table 6

Summary of results from the partitioned UQ analysis of a spherical 440c stainless steel projectiles/6061-T6 aluminum plate system. Plate thicknesses are in the range [2.2 mm, 3.2 mm], obliquities in the range [0°, 30°] and impact velocities in the range [2.4 km/s, 2.8 km/s]. For purposes of the partitioned analysis, the obliquity range is partitioned into two sub-ranges, [0°, 15°] and [15°, 30°].

Variable range	$\alpha \in [0^\circ, 15^\circ]$	$\alpha \in [15^\circ, 30^\circ]$
Model diameter $D_{\langle F \rangle}$		
Thickness	3.46 mm ²	1.77 mm ²
Obliquity	3.42 mm ²	1.84 mm ²
Total	4.86 mm ²	2.56 mm ²
Model diameter $D_{\langle F-G \rangle}$		
Thickness	3.52 mm ²	2.82 mm ²
Obliquity	2.62 mm ²	2.04 mm ²
Total	4.39 mm ²	3.48 mm ²
$D_{\langle F \rangle} + D_{\langle F-G \rangle}$	9.25 mm ²	6.04 mm ²
Empirical mean $\mathbb{E}_m[G]$, $m=100$	11.2 mm ²	11.11 mm ²
Margin hit α ($\epsilon' = 1\%$)	1.59 mm ²	1.1 mm ²
Experimental scatter D_Z	3.89 mm ²	
Sub- confidence factor M/U	0.96	1.39
Sub-PoF upper bound	15.8%	2.1%
PoF upper bound	8.95%	

illustrate the partitioned analysis simply by bisecting the range for impact obliquity into two sub-ranges, [0°, 15°] and [15°, 30°], which we assume to be equiprobable; the other input parameter ranges are left unchanged. The McDiarmid diameters and empirical means of $\langle F \rangle$ and $\langle F-G \rangle$ are calculated as before on each of these two ranges. The probability of non-perforation then satisfies the upper bound

$$\mathbb{P}[G(h, \alpha, v) \leq 0] \leq \sum_{i=1}^2 \mathbb{P}(A_i) \exp\left(-\frac{2(\langle G \rangle - \alpha_\epsilon)_+^2}{(D_{\langle F \rangle} + D_{\langle F-G \rangle})^2 + D_Z^2}\right) \quad (34)$$

where $A_1 = [2.2 \text{ mm}, 3.2 \text{ mm}] \times [0^\circ, 15^\circ] \times [2.4 \text{ km/s}, 2.8 \text{ km/s}]$ and $A_2 = [2.2 \text{ mm}, 3.2 \text{ mm}] \times [15^\circ, 30^\circ] \times [2.4 \text{ km/s}, 2.8 \text{ km/s}]$. This partitioned UQ analysis is summarized in Table 6. As may be seen from the table, a simple two-way partitioning of the obliquity range reduces the probability-of-failure upper bound from 16.2% to 8.95%. Indeed, Sullivan et al. (2011) have shown that a sequential bisection procedure generates a sequence of probability-of-failure upper bounds that converges to the exact probability of failure in the limit.

4. Summary and concluding remarks

The UQ case study presented in the foregoing is concerned with the assessment of the feasibility of an *extended data-on-demand* (XDoD) UQ protocol based on concentration-of-measure probability-of-failure inequalities and martingale theory. The XDoD UQ protocol extends the data-on-demand (DoD) UQ protocol presented in Part I of this series and enables consideration of systems with uncontrollable inputs and non-negligible experimental scatter. The assessment is based on an experimental configuration consisting of 6061-T6 aluminum plates struck spherical 440c stainless steel projectiles at ballistic impact speeds in the range of 2.4–2.8 km/s. The system's inputs are the plate thickness, the plate obliqueness and impact velocity and, for simplicity, the perforation area is chosen as the sole performance measure of the system. The objective of the UQ analysis is to certify the lethality of the projectile, i.e., that the projectile perforates the plate with high probability over a prespecified range of impact velocities and plate thicknesses.

All the data used in the UQ analysis was acquired at Caltech's Small Particle Hypervelocity Range (SPHIR), which houses a two-stage gas gun. A peculiarity of the SPHIR facility, which has partly provided impetus for the theoretical developments presented in this Part II, is that the impact velocity, while amenable to precise measurement, cannot be controlled precisely but varies randomly according to an ostensibly uniform probability density function. In addition, due to a competition between petalling and plugging mechanisms for the material system under consideration, the measured perforation area exhibits considerable scatter. The need to deal effectively with noisy data presents challenges that go beyond the simple DoD UQ protocol and motivates the extensions presented in this Part II.

All simulations in support of the UQ analysis were carried out using the Optimal-Transportation MeshFree (OTM) method (Li et al., 2010) extended to account for contact and fracture (Schmidt et al., 2009) in order to simulate terminal ballistics (cf. also Li et al., 2011). The materials are described by means of engineering viscoplasticity models with power-law hardening, rate-sensitivity and thermal softening combined with a Mie-Grüneisen equation of state. In order to capture the upturn in rate-sensitivity that is experimentally observed to occur in 440c stainless steel beyond a transition strain rate of $2 \times 10^5 \text{ s}^{-1}$, we adopt a two-stage rate-sensitivity law (Marusich and Ortiz, 1995).

The calculation of all diameters was carried out using lattice-Powell's method (Powell, 1989, 1994). The Powell calculations converged in the order of 8 iterations, requiring a total of 96 experiments, or 96 evaluations of the response function. As in Part I, the requisite number of experiments is within the realm of feasibility, especially considering that the

number of inputs is now 3 instead of 2. In general, the complexity of the analysis and the number of experiments required may be expected to scale with the number of parameters as the optimization algorithm used in the calculation of the diameters. If the modeling error function $G-F$ is sufficiently small and well-behaved, as expected from a high-fidelity model, rapidly convergent iterative algorithms should be applicable, resulting in polynomial complexity. Thus, the present UQ protocol, and specifically the quantification of uncertainties through diameters, is free of the *curse of dimensionality* that afflicts other methods, e.g., those based on direct sampling, which suffer from combinatorial complexity.

For the system under consideration, the net outcome of the model-based XDoD UQ analysis is a low confidence factor of $M/U=0.95$, or a probability-of-failure upper bound of 16.2%. By contrast, an analysis based directly on test data gives a substantially higher confidence factor $M/U=1.44$ and a substantially lower probability-of-failure upper bound of 2%. It bears emphasis that the main reason why the model-based analysis is lax is that the modeling error is high. This outcome is not entirely unexpected since the material constants used in the OTM calculations are of archival extraction and no effort has been made to calibrate the model. Given the large number of material constants and other model parameters, a modicum of calibration is likely to bring the model in closer alignment with experiment and lower the modeling-error diameter as a result. A more satisfactory approach would be to calibrate the model based on material data representative of the conditions of the experiment, which should likely result in a reduction of the modeling-error diameter.

These improvements notwithstanding, a systematic reduction of modeling errors invariably necessitates the formulation of higher-fidelity models. Indeed, the simple engineering models employed in the present analysis are amenable to a number of improvements. Thus, the experimental evidence is suggestive of melting around the perforation of the plate, an effect whose modeling requires more accurate accounting of thermal effects and phase transitions than considered in the present work. Another effect that calls for higher-fidelity modeling is the fragmentation of the projectile. Thus, within the range of the UQ analysis, the fracture of the stainless steel 440c projectile undergoes a transition from ductile to brittle. Despite the two-stage power-law adopted to describe the rate-sensitivity of the material, the ductile-to-brittle transition is not sufficiently well-captured by the model. Multiscale models suggest themselves as an avenue for systematically improving on the fidelity of material models, albeit often at the expense of considerable added computational cost.

Another source of over-conservatism stems from the reliance on the simple McDiarmid bound. On way of improving on this bound is by recourse to the *partitioned* UQ analysis of Sullivan et al. (2011). In this approach, the domain of the input parameters is partitioned recursively and local McDiarmid bounds are computed for each partition. The method generates a sequence of bounds that converges from above to the exact probability-of-failure of the system. In this manner, the probability-of-failure bounds can be rendered as tight as desired, albeit at a concomitant increase in the computational and experimental effort. Another avenue for tightening the bounds is by recourse to *optimal uncertainty quantification* (OUQ) (Owhadi et al., 2010). Thus, the fact that McDiarmid's inequality is not the tightest bound that can be constructed from diameters and mean performance values has already noted in Part I of this series, where optimal bounds are also given.

Acknowledgments

The authors gratefully acknowledge the support of the Department of Energy National Nuclear Security Administration under Award Number DE-FC52-08NA28613 through Caltech's ASC/PSAAP Center for the Predictive Modeling and Simulation of High Energy Density Dynamic Response of Materials.

Appendix A. A theorem from martingale theory

For completeness, we include in this section the main result from martingale theorem from which Theorem 2.1 is derived. The theorem follows directly from Theorem 2.3 of McDiarmid (1997) (we also refer to the Theorem (6.7) and corollary (6.9) of McDiarmid, 1989b).

Theorem A.1. Let $\mathcal{F}_0 \subseteq \mathcal{F}_1 \subseteq \dots \subseteq \mathcal{F}_n$ be a filtration where \mathcal{F}_0 is the trivial σ -algebra. Let the integrable random variable V be \mathcal{F}_n -measurable, and let V_0, V_1, \dots, V_n be the martingale obtained by setting $V_k := \mathbb{E}[V | \mathcal{F}_k]$. Suppose that for each $k=1, \dots, n$ there are constants a_k, b_k , such that we have $a_k \leq V_k - V_{k-1} \leq b_k$. Then, for any $t > 0$, we have \mathbb{P} -almost surely,

$$\mathbb{P}[V_n - \mathbb{E}[V] \geq t] \leq \exp\left(-2 \frac{t^2}{\sum_{k=1}^n (b_k - a_k)^2}\right) \quad (\text{A.1})$$

and

$$\mathbb{P}[V_n - \mathbb{E}[V] \leq -t] \leq \exp\left(-2 \frac{t^2}{\sum_{k=1}^n (b_k - a_k)^2}\right) \quad (\text{A.2})$$

Let G be a function of the random vector $X := (X_1, \dots, X_N)$. Choosing $V := G(X_1, \dots, X_N)$ and $\mathcal{F}_k := \sigma(X_1, \dots, X_k)$ we obtain, as an application of Theorem A.1, that, if for each $k=1, \dots, N$ there are constants a_k, b_k , such that we have $a_k \leq \mathbb{E}$

$[G(X)|X_1, \dots, X_k] - \mathbb{E}[G(X)|X_1, \dots, X_{k-1}] \leq b_k$. Then, for any $t > 0$, we have \mathbb{P} -almost surely,

$$\mathbb{P}[G(X) - \mathbb{E}[G(X)] \geq t] \leq \exp\left(-2 \frac{t^2}{\sum_{k=1}^n (b_k - a_k)^2}\right) \tag{A.3}$$

and

$$\mathbb{P}[G(X) - \mathbb{E}[G(X)] \leq -t] \leq \exp\left(-2 \frac{t^2}{\sum_{k=1}^n (b_k - a_k)^2}\right) \tag{A.4}$$

Appendix B. The experimental-scatter diameter in the Gaussian case

The following theorem addresses the case of Gaussian experimental scatter and provides an appropriate working definition of the experimental-scatter diameter. We start by recalling the following lemma from [Hoeffding \(1963\)](#), cf. also Lemma 3.2 of [McDiarmid \(1997\)](#).

Lemma B.1. *Let X be a real-valued random variable with $\mathbb{E}[X] = \mu$ and $a \leq X \leq b$ where a and b are constants. Then for any $h \in \mathbb{R}$,*

$$\mathbb{E}[e^{hX}] \leq \frac{b-\mu}{b-a} e^{ha} + \frac{\mu-b}{b-a} e^{hb} \leq e^{h\mu} \exp\left(\frac{1}{8} h^2 (b-a)^2\right) \tag{B.1}$$

Recall that we denote by $\langle G \rangle(X)$ the probability average of $G(X,Z)$ with respect to Z , and by $\rho(X,Z)$ the scatter function (18). Then, we have the following.

Theorem B.2. *Suppose that $\langle G \rangle(X)$ and ρ are independent and that ρ is a Gaussian random variable with variance σ^2 . Then,*

$$\mathbb{P}[G(X,Z) \geq r] \leq \exp\left(-2 \frac{(r - \mathbb{E}[G])_+^2}{D_{\langle G \rangle}^2 + 4\sigma^2}\right) \tag{B.2}$$

and

$$\mathbb{P}[G(X,Z) \leq r] \leq \exp\left(-2 \frac{(\mathbb{E}[G] - r)_+^2}{D_{\langle G \rangle}^2 + 4\sigma^2}\right) \tag{B.3}$$

Proof. Theorem B.2 follows from a simple modification of the proof of the martingale concentration inequality ([McDiarmid, 1997](#)). Using the notations of [Theorem A.1](#), we let \mathcal{F}_0 be the trivial σ -algebra, \mathcal{F}_k the σ -algebra generated by X_1, \dots, X_k ($1 \leq k \leq N$) and \mathcal{F}_{N+1} the σ -algebra generated by X_1, \dots, X_N, Z . We introduce the martingale defined by

$$V_k = \mathbb{E}[G(X,Z) | \mathcal{F}_k] \tag{B.4}$$

for $k=0, \dots, N+1$. From Markov's inequality we have, for $h > 0$,

$$\mathbb{P}[V_{N+1} - \mathbb{E}[V_{N+1}] \geq r] \leq e^{-hr} \mathbb{E}[\exp(h(V_{N+1} - \mathbb{E}[V_{N+1}]))] \tag{B.5}$$

Since (\mathcal{F}_k) is a filtration,

$$\mathbb{E}[\exp(h(V_{N+1} - \mathbb{E}[V_{N+1}]))] = \mathbb{E}[e^{h(V_N - \mathbb{E}[V_{N+1]})}] \mathbb{E}[e^{h(V_{N+1} - V_N)} | \mathcal{F}_N] \tag{B.6}$$

Since $V_{N+1} - V_N = \rho$ is a Gaussian of variance σ^2 independent from \mathcal{F}_N , we have

$$\mathbb{E}[e^{h(V_{N+1} - V_N)} | \mathcal{F}_N] = \mathbb{E}[e^{h\rho}] = \exp\left(\frac{1}{2} h^2 \sigma^2\right) \tag{B.7}$$

Hence

$$\mathbb{P}[V_{N+1} - \mathbb{E}[V_{N+1}] \geq r] \leq e^{-hr + 1/2h^2\sigma^2} \mathbb{E}[\exp(h(V_N - \mathbb{E}[V_{N+1}]))] \tag{B.8}$$

Similarly,

$$\mathbb{E}[\exp(h(V_N - \mathbb{E}[V_{N+1}]))] = \mathbb{E}[e^{h(V_{N-1} - \mathbb{E}[V_{N+1]})}] \mathbb{E}[e^{h(V_N - V_{N-1})} | \mathcal{F}_{N-1}] \tag{B.9}$$

By [Lemma B.1](#), using the notations of [Theorem A.1](#), we have \mathbb{P} -almost surely,

$$\mathbb{E}[e^{h(V_N - V_{N-1})} | \mathcal{F}_{N-1}] \leq \exp\left(\frac{1}{8} h^2 (b_N - a_N)^2\right) \tag{B.10}$$

It then follows that

$$\mathbb{P}[V_{N+1} - \mathbb{E}[V_{N+1}] \geq r] \leq e^{-hr + 1/8h^2(4\sigma^2 + (b_N - a_N)^2)} \mathbb{E}[\exp(h(V_N - \mathbb{E}[V_{N+1}]))] \tag{B.11}$$

By induction,

$$\mathbb{P}[V_{N+1} - \mathbb{E}[V_{N+1}] \geq r] \leq e^{-hr+1/8h^2(4\sigma^2 + \sum_{k=1}^N (b_k - a_k)^2)} \quad (\text{B.12})$$

The proof of (B.2) follows by taking $h = 4r/(4\sigma^2 + \sum_{k=1}^N (b_k - a_k)^2)$ and observing that $\sum_{k=1}^N (b_k - a_k)^2 = D_{<G}^2$ and that $V_{N+1} = G(X, Z)$. \square

References

- Boucheron, S., Bousquet, O., Lugosi, G., 2004a. Concentration inequalities. In: Bousquet, O., Luxburg, U., Rätsch, G. (Eds.), *Advanced Lectures in Machine Learning*, Springer, pp. 208–240.
- Boucheron, S., Bousquet, O., Lugosi, G., 2004b. Concentration inequalities. In: *Advanced Lectures in Machine Learning*, Springer, pp. 208–240.
- Camacho, G.T., Ortiz, M., 1997. Adaptive lagrangian modelling of ballistic penetration of metallic targets. *Comput. Methods Appl. Mech. Eng.* 142, 269–301.
- Clifton, R., Klopp, R., 1985. Pressure–shear plate impact testing. In: *Metals Handbook 9th Edition* (8), pp. 230–239.
- Hodowany, J., Ravichandran, G., Rosakis, A.J., Rosakis, P., 2000. Partition of plastic work into heat and stored energy in metals. *Exp. Mech.* 40 (2), 113–123.
- Hoeffding, W., 1963. Probability inequalities for sums of bounded random variables. *J. Am. Stat. Assoc.* 58, 13–30.
- Klopp, R., Clifton, R., Shawki, T., 1985. Pressure–shear impact and the dynamic viscoplastic response of metals. *Mech. Mater.* 4, 375–385.
- Ledoux, M., 2001. The concentration of measure phenomenon. *Mathematical Surveys and Monographs*, vol. 89. , American Mathematical Society.
- Li, B., Habbal, F., Ortiz, M., 2010. Optimal transportation meshfree approximation schemes for fluid and plastic flows. *Int. J. Numer. Methods Eng.* 83 (12), 1541–1579.
- Li, B., Kidane, A., Ravichandran, G., Ortiz, M., 2012. Verification and validation of the Optimal Transportation Meshfree (OTM) Simulation of Terminal Ballistics. *Int. J. Impact Eng.* 42, 25–36.
- Lucas, L.J., Owahdi, H., Ortiz, M., 2008. Rigorous verification, validation, uncertainty quantification and certification through concentration-of-measure inequalities. *Comput. Methods Appl. Mech. Eng.* 197, 4591–4609.
- Lugosi, G., 2006. Concentration-of-measure inequalities. Lecture notes. <<http://www.econ.upf.edu/~lugosi/anu.pdf>>.
- Marusich, T., Ortiz, M., 1995. Modeling and simulation of high-speed machining. *Int. J. Numer. Methods Eng.* 38 (21), 3675–3694.
- McDiarmid, C., 1989a. On the method of bounded differences. *Surveys in Combinatorics*, London Mathematical Society Lecture Notes Series, vol. 141. Cambridge University Press, pp. 148–188.
- McDiarmid, C., 1989b. On the method of bounded differences. *Surveys in Combinatorics*, 1989 (Norwich, 1989). London Mathematical Society Lecture Notes Series, vol. 141. , Cambridge University Press, Cambridge, pp. 148–188.
- McDiarmid, C., 1997. Centering sequences with bounded differences. *Combin. Probab. Comput.* 6 (1), 79–86.
- McDiarmid, C., 1998. Concentration. *Probabilistic Methods for Algorithmic Discrete Mathematics*. Algorithms Combine, vol. 16. , Springer, Berlin, pp. 195–248.
- McKerns, M.P.H., Aivazis, M., 2010. Mystic: a simple model-independent inversion framework. <<http://dev.danse.us/trac/mystic>>.
- Owahdi, H., Scovel, C., Sullivan, T., McKerns, M., Ortiz, M., 2010. Optimal uncertainty quantification. arXiv:1009.0679v1.
- Powell, M.J.D., 1989. A tolerant algorithm for linearly constrained optimization calculations. *Math. Programming* 45, 547–566.
- Powell, M.J.D., 1994. A direct search optimization method that models the objective and constraint functions by linear interpolation. In: Gomez, S., Hennart, J.P. (Eds.), *Advances in Optimization and Numerical Analysis*, Kluwer Academic, Dordrecht, pp. 51–67.
- Schmidt, B., Fraternali, F., Ortiz, M., 2009. Eigenfracture: an eigendeformation approach to variational fracture. *Multiscale Model. Simul.* 7, 1237–1266.
- Stainier, L., Ortiz, M., 2010. Study and validation of a variational theory of thermo-mechanical coupling in finite visco-plasticity. *Int. J. Solids Struct.* 47, 705–715.
- Sullivan, T.J., Topcu, U., McKerns, M., Owahdi, H., 2011. Uncertainty quantification via codimension-one partitioning. *Int. J. Numer. Methods Eng.* 85 (12), 1499–1521. <<http://dx.doi.org/10.1002/nme.3030>>.
- Tong, W., Clifton, R., Huang, S., 1992. Pressure–shear impact investigation of strain rate history effects in oxygen-free high-conductivity copper. *J. Mech. Phys. Solids* 40, 1251–1294.
- Yadav, S., Chichili, D., Ramesh, K., 1995. The mechanical response of a 6061-T6 Al/Al₂O₃ metal matrix composite at high rates of deformation. *Acta Metall. Mater.* 43 (12), 4453–4464.
- Yadav, S., Repetto, E., Ravichandran, G., Ortiz, M., 2001. A computational study of the influence of thermal softening on ballistic penetration in metals. *Int. J. Impact Eng.* 25 (8), 787–803.
- Yang, Q., Stainier, L., Ortiz, M., 2006. A variational formulation of the coupled thermo-mechanical boundary-value problem for general dissipative solids. *J. Mech. Phys. Solids* 54, 401–424.